Momentum distribution and correlation of two-nucleon relative motion in ^{6}He and ^{6}Li

W. Horiuchi[1] and Y. Suzuki[2]
[1]*Graduate School of Science and Technology, Niigata University, Niigata 950-2181, Japan*
[2]*Department of Physics, and Graduate School of Science and Technology, Niigata University, Niigata 950-2181, Japan*
(Received 17 April 2007; published 10 August 2007)

The momentum distribution of relative motion between two nucleons gives information on the correlation in nuclei. The momentum distribution is calculated for both ^{6}He and ^{6}Li, which are described in a three-body model of $\alpha + N + N$. The ground-state solution for the three-body Hamiltonian is obtained accurately using correlated basis functions. The momentum distribution depends on the potential model for the N-N interaction. With use of a realistic potential, the ^{6}He momentum distribution exhibits a dip around 2 fm^{-1} characteristic of S-wave motion. In contrast to this, the ^{6}Li momentum distribution is very similar to that of the deuteron; no dip appears because it is filled with the D-wave component arising from the tensor force.

DOI: 10.1103/PhysRevC.76.024311 PACS number(s): 27.20.+n, 21.60.−n, 25.60.Gc, 21.10.Gv

I. INTRODUCTION

In this article we study the momentum distribution and the correlation of relative motion of the neutrons in two-neutron halo nuclei. The importance of the correlation in nuclei is widely recognized; obviously the correlation plays a vital role in binding a Borromean three-body system that has no pairwise bound states. Recently an experiment using the technique of intensity interferometry [1] has been done to extract the spatial correlation function of the two neutrons in the halo nuclei such as ^{6}He, ^{11}Li, and ^{14}Be. In this experiment the momenta of the two neutrons and the core nucleus are measured after the dissociation of the halo nucleus.

Another type of experiment has very recently been performed at RIKEN to probe the spatial correlation in ^{6}He and ^{6}Li, and the analysis of data is in progress [2]. The basic idea of this experiment is to utilize the well-established one-nucleon exchange process that is observed at the backward angle in the proton-deuteron elastic scattering [3]. Expecting this mechanism to occur in the interaction of the $A = 6$ nuclei with a proton, the cross section for the reaction ^{6}He$(p, dn)\alpha$ (^{6}Li$(p, dp)\alpha$) has been measured under the backward-scattering kinematics of the proton and two-nucleon system in ^{6}He (^{6}Li). Under the assumption of a quasielastic approximation, the cross section is expected to be sensitive to the relative momentum between the two nucleons [4]. Though the reaction mechanism may not be as simple as expected, a theoretical analysis of the momentum distribution in ^{6}He and ^{6}Li should be important as a first step to understand the physics involved in the experiment.

There are a number of calculations for the structure of ^{6}He in various models. We employ a three-body model of $\alpha + N + N$ for ^{6}He and ^{6}Li. It will be important for our purpose to use a realistic potential for the interaction between the valence nucleons because the correlation between them is primarily determined by the N-N potential and the distribution at high momentum should be sensitive to the short-ranged repulsion and tensor force. We refer to Refs. [5,6] as the most relevant calculations which include the tensor force. However, nothing in the literature has considered the momentum distribution between the valence nucleons. There are, of course, many studies that have investigated the momentum distribution of fragments such as the core nucleus or the nucleon [7].

This article is organized as follows. In Sec. II we present our three-body model and some of the details on explicitly correlated basis functions that are used to solve the three-body problem. Some formulas needed to compare ^{6}He and ^{6}Li properties are given in this section with emphasis on the two-nucleon correlation function and the momentum distribution. The latter is best defined through the Wigner distribution function [8]. One well-known formulation of single-nucleon momentum distribution near nuclear surface was performed by Hüfner and Nemes [9] using the Wigner function. Results of calculation are presented in Sec. III together with some discussions. Those included are the spectroscopic properties, the two-nucleon correlation functions that reveal "dineutron" as well as "cigar-like" configurations and the comparison of the momentum distributions. We will show that the tensor force that works differently between ^{6}He and ^{6}Li plays a key role in the momentum distribution around 2 fm^{-1}. A conclusion is given in Sec. IV. In Appendix A, we derive the formulas of calculating charge and matter radii in a three-body model. In Appendix B we give a formula to calculate a density matrix or the Wigner function using the correlated basis functions.

II. FORMULATION

A. Three-body Hamiltonian

The wave functions for ^{6}He and ^{6}Li are determined from variational calculations for the core (α particle) $+N + N$ three-body system, which is specified by the Hamiltonian

$$H = T_{\boldsymbol{r}} + T_{\boldsymbol{R}} + U_1 + U_2 + v_{12}\,. \tag{1}$$

The subscripts of the kinetic energies T stand for the relative distance vector $\boldsymbol{r}$ between the two nucleons, and the relative distance vector $\boldsymbol{R}$ from the α particle to the center-of-mass of the two nucleons. The set of Jacobi coordinates $(\boldsymbol{r}, \boldsymbol{R})$ is called T-type hereafter. The potential U_i is the N-α potential and v_{12} is the N-N potential. The α particle is treated as a structureless particle.

 ©2007 The American Physical Society

As the two-nucleon potential v_{12}, we use a realistic potential, G3RS (Gaussian soft core potential with 3 ranges) case 1 potential [10], which contains central (C), spin-orbit (LS), and tensor (T) terms. In fact, the G3RS potential contains $\boldsymbol{L}^2$ and quadratic $\boldsymbol{L}\cdot\boldsymbol{S}$ terms in even L waves. Their contribution is small; the deuteron energy with (without) these terms is -2.17 (-2.28) MeV. Thus we ignore these L-dependent terms in what follows. The D state probability of the deuteron is 4.8 % in the G3RS potential. We use the G3RS potential because its Gaussian radial form makes a numerical calculation much faster than, e.g., the AV8′ potential [11]. It is instructive for the study of the N-N correlated motion to compare results of calculation between the realistic potential model and an effective potential model that has a mild short-ranged repulsion. As such an effective potential we employ the Minnesota potential [12], abbreviated to MN, which has no tensor component. This potential renormalizes the effect of the tensor force into the central force and reproduces the binding energy and the root-mean-square (rms) radius of the deuteron.

As for the N-α potential U_i, we adopt a phenomenological potential [13], abbreviated to KKNN potential, which is determined so as to simulate the nonlocal potential that derives from a microscopic calculation in an $N+\alpha$ cluster model. The KKNN potential is parity dependent, contains the central and spin-orbit components, and reproduces very well the low-energy N-α scattering phase shifts of S and P waves. The potential is slightly too repulsive in D and F waves [14]. The Coulomb potential for p-α is taken as

$$U^{\rm Coul}(r)=\frac{2e^2}{r}\,{\rm erf}\left(\sqrt{\frac{4}{3b^2}}r\right), \tag{2}$$

with $\frac{1}{2b^2}=0.257$ fm^{-2}. The KKNN potential is deep enough to support an S-wave bound state; the state is considered redundant and must be removed in the three-body calculation because no bound states exist for ^{5}He and ^{5}Li.

B. Variational solution with correlated Gaussians

Trial wave functions for the ground states of ^{6}He and ^{6}Li are expressed, in LS coupling scheme, as a combination of explicitly correlated Gaussians:

$$\Psi_{JM}=\sum_{i=1}^{K}C_i\Psi_{JM}(\Lambda_i,A_i,u_i), \tag{3}$$

with the basis function

$$\Psi_{JM}(\Lambda=(LS),A,u,\boldsymbol{x}) =(1-P_{12})\left\{{\rm e}^{-\frac{1}{2}\tilde{\boldsymbol{x}}A\boldsymbol{x}}[\mathcal{Y}_L(\tilde{u}\boldsymbol{x})\chi_S(1,2)]_{JM}\eta_{TM_T}(1,2)\right\}. \tag{4}$$

Here the permutation P_{12} ensures the antisymmetry of the valence nucleons.

The basis function is specified by a set of nonlinear parameters, the orbital and spin angular momenta $\Lambda=(LS)$, a 2×2 positive-definite, symmetric matrix A, and a 2×1 matrix u. The symbol $\tilde{}$ indicates the transpose of a matrix, and the square bracket $[\mathcal{Y}_L\chi_S]$ denotes the angular momentum coupling. The short-hand notation $\tilde{\boldsymbol{x}}A\boldsymbol{x}$ with $\tilde{\boldsymbol{x}}=(\boldsymbol{x}_1,\boldsymbol{x}_2)$ stands for $A_{11}\boldsymbol{x}_1^2+2A_{12}\boldsymbol{x}_1\cdot\boldsymbol{x}_2+A_{22}\boldsymbol{x}_2^2$, where the coordinates $\boldsymbol{x}_1$ and $\boldsymbol{x}_2$, called V-type, are the distance vectors of the valence nucleons from the α particle; $\boldsymbol{x}_1=\boldsymbol{R}+\frac{1}{2}\boldsymbol{r}$ and $\boldsymbol{x}_2=\boldsymbol{R}-\frac{1}{2}\boldsymbol{r}$. The exponential part of the basis function is rotation invariant. The cross term $A_{12}\boldsymbol{x}_1\cdot\boldsymbol{x}_2$ describes explicitly the two-nucleon correlation, which is vital to obtain a precise solution in a relatively small basis dimension [15]. The angular part of the basis function is expressed by the solid spherical harmonics, $\mathcal{Y}_{LM_L}(\tilde{u}\boldsymbol{x})=|\tilde{u}\boldsymbol{x}|^L Y_{LM_L}(\widehat{\tilde{u}\boldsymbol{x}})$, specified by a global vector $\tilde{u}\boldsymbol{x}=u_1\boldsymbol{x}_1+u_2\boldsymbol{x}_2$. The ratio of u_1 to u_2 characterizes the coordinate that is responsible for the rotation of the system [15,16]. (The norm of u, $u_1^2+u_2^2$, simply affects the normalization of the basis function but not the rotation itself, and it may be set to unity.) The isospin part of the system is expressed by η_{TM_T}. The p-α Coulomb potential and the neutron-proton mass difference give rise to the isospin impurity in ^{6}Li, but its effect is rather small [17,18]. We ignore the neutron-proton mass difference and consider no isospin mixing in the present study. The action of P_{12} on the basis function is simple; it maintains the functional form [15,19] as follows:

$$P_{12}{\rm e}^{-\frac{1}{2}\tilde{\boldsymbol{x}}A\boldsymbol{x}}[\mathcal{Y}_L(\tilde{u}\boldsymbol{x})\chi_S(1,2)]_{JM}\eta_{TM_T}(1,2) =(-1)^{S+T}{\rm e}^{-\frac{1}{2}\tilde{\boldsymbol{x}}\bar{A}\boldsymbol{x}}[\mathcal{Y}_L(\tilde{\bar{u}}\boldsymbol{x})\chi_S(1,2)]_{JM}\eta_{TM_T}(1,2), \tag{5}$$

where the symbol $\bar{}$ indicates the interchange of the elements of the matrix, that is, $\bar{A}_{11}=A_{22}$, $\bar{A}_{12}=\bar{A}_{21}=A_{12}$, $\bar{A}_{22}=A_{11}$ and $\bar{u}_1=u_2$, $\bar{u}_2=u_1$.

A conventional choice for describing the rotational motion is a partial wave expansion, $[\mathcal{Y}_{\ell_1}(\boldsymbol{x}_1)\mathcal{Y}_{\ell_2}(\boldsymbol{x}_2)]_{LM_L}$. One introduces a set of important partial waves $(\ell_1\ell_2)$ to obtain a converged solution [5,20]. See also Ref. [17] for the importance of including high partial waves in the Faddeev calculation for ^{6}Li. Our angular function looks quite different from this and it is much simpler than the partial wave expansion. No apparent couplings appear, and the use of the global vector greatly simplifies the calculation of the Hamiltonian matrix elements [15,16]. The merit of this angular function lies not only in its simplicity but also in its performance. As was compared in Ref. [16], the global vector representation gives results as accurately as the partial wave expansion. With use of the decomposition

$$\mathcal{Y}_{LM_L}(u_1\boldsymbol{x}_1+u_2\boldsymbol{x}_2)=\sum_{\ell=0}^{L}\sqrt{\frac{4\pi(2L+1)!}{(2\ell+1)!(2L-2\ell+1)!}} \times u_1^{\ell}u_2^{L-\ell}[\mathcal{Y}_{\ell}(\boldsymbol{x}_1)\mathcal{Y}_{L-\ell}(\boldsymbol{x}_2)]_{LM_L}, \tag{6}$$

the partial waves $(\ell_1\ell_2)$ contained in the global vector part are only $(0L),(1L-1),\ldots,(L0)$. A very important point of our basis function is that other necessary partial wave contributions are brought about by the $\exp(-A_{12}\boldsymbol{x}_1\cdot\boldsymbol{x}_2)$ term. When the term is expanded as $\sum_n[(-A_{12})^n/n!](\boldsymbol{x}_1\cdot\boldsymbol{x}_2)^n$, each term in the series produces the partial wave components of type, $(x_1x_2)^{n-\lambda}[\mathcal{Y}_\lambda(\boldsymbol{x}_1)\mathcal{Y}_\lambda(\boldsymbol{x}_2)]_{00}$ with $\lambda=n,n-2,\ldots,1$ or 0. When this is combined with $[\mathcal{Y}_\ell(\boldsymbol{x}_1)\mathcal{Y}_{L-\ell}(\boldsymbol{x}_2)]_{LM_L}$ coming from the global vector part, it is clear that the basis function (4) can practically contain important partial wave combinations.

We note that the basis function of Eq. (4) has a definite parity $(-1)^L$. As the ground states of ^{6}He and ^{6}Li have a

positive parity, this basis function cannot be used for $L = 1$. We need to extend the basis function to make it possible to include $L = 1$ and a positive parity. This is made possible by replacing $\mathcal{Y}_{LM_L}(\tilde{u}\boldsymbol{x})$ by $[\mathcal{Y}_L(\tilde{u}\boldsymbol{x})\mathcal{Y}_1(\tilde{u'}\boldsymbol{x})]_{LM_L}$ [21]. For the case of two nucleons with $L = 1$, this replacement results in a new basis function

$$\Psi_{JM}(\Lambda = (1S), A, \boldsymbol{x}) = (1 - P_{12})\Big\{e^{-\frac{1}{2}\tilde{\boldsymbol{x}}A\boldsymbol{x}}[[\mathcal{Y}_1(\boldsymbol{x}_1)\mathcal{Y}_1(\boldsymbol{x}_2)]_1 \times \chi_S(1,2)]_{JM}\eta_{TM_T}(1,2)\Big\}. \quad (7)$$

Note that $[\mathcal{Y}_1(\boldsymbol{x}_1)\mathcal{Y}_1(\boldsymbol{x}_2)]_1$ is equal to the vector product $\boldsymbol{x}_1 \times \boldsymbol{x}_2$ within a constant factor. The operation of P_{12} can be done as in Eq. (5), with an extra minus sign coming from this vector coupling.

The set of $\Lambda = (LS)$ included in the present calculation is summarized as follows:

$$\begin{aligned} &\text{For } {}^6\text{He}(J^\pi = 0^+), \quad (LS) = (00), (11). \\ &\text{For } {}^6\text{Li}(J^\pi = 1^+), \quad (LS) = (01), (10), (11), (21). \end{aligned} \quad (8)$$

Here the basis function is given by Eq. (4) for even L and by Eq. (7) for odd L, respectively. Note that the two independent $L = 1$ basis states exist for ^{6}Li.

As noted before, the redundant state of the KKNN potential has to be eliminated; this elimination is a manifestation of the Pauli principle for the motion of the valence nucleons. The requirement is met by imposing that the trial wave function has no overlap with the $0s_{1/2}$ bound state of the KKNN potential:

$$\left\langle 0s_{\frac{1}{2}m m_3}(i)\middle|\Psi_{JM}\right\rangle = 0 \quad (i = 1, 2), \quad (9)$$

where the radial coordinate of the $0s_{1/2}$ function is $\boldsymbol{x}_i$ and m_3 is the third component of the isospin of the nucleon i. The $0s_{1/2}$ bound-state wave functions for the neutron and the proton are only slightly different because of the Coulomb potential, and thus we ignore their difference in the present calculation. The exclusion of the $0s_{1/2}$ component is practically achieved by the orthogonal projection method [22]. That is, we add in the three-body Hamiltonian (1) a nonlocal, pseudopotential,

$$\gamma \sum_{i=1}^{2} \sum_{m=\pm\frac{1}{2}} \left|0s_{\frac{1}{2}m m_3}(i)\right\rangle\left\langle 0s_{\frac{1}{2}m m_3}(i)\right|, \quad (10)$$

and obtain a stable solution for sufficiently large γ (typically 10^6 MeV or larger than that).

To search for good basis functions, we use the algorithm called the stochastic variational method (SVM) [15]. The SVM increases the basis dimension one by one by testing a number of candidates that are chosen randomly. Because each basis function is specified by the parameters $(A_{11}, A_{12}, A_{22}, u_1)$ or (A_{11}, A_{12}, A_{22}), the candidates are actually generated by giving random numbers to the parameters chosen from physically important multidimensional parameter space. In this way we determine about 100–200 basis functions for each Λ. The SVM works efficiently to take care of both the short-ranged repulsion of the realistic force and the elimination of the redundant states.

C. Transformation of coordinate sets

In the Faddeev method for a three-body system, three sets of T-type Jacobi coordinates are used, and each Faddeev component of the total wave function, expressed in one of the three sets, is expanded in partial waves. To specify the basis function, however, we use the V-type coordinate $\boldsymbol{x}$, which is different from the T-type coordinate. The V-type coordinate is a set of "single particle"- (s.p.) like coordinate, and it is chosen to make it easy to implement the symmetry of the nucleons. See Eq. (5). The s.p. coordinate is useful to represent the individual motion of the nucleons when the correlation term vanishes, i.e., A_{12} is set to zero. For example, the 0^+ ground-state wave function of ^{6}He, approximated in p-shell harmonic-oscillator configurations, will be expressed in terms of a combination of the spin-singlet and spin-triplet states

$$\begin{aligned} \Phi_0 &= \mathcal{N}_0 e^{-\frac{1}{2}a_0(\boldsymbol{x}_1^2+\boldsymbol{x}_2^2)} \\ &\quad \times [[\mathcal{Y}_1(\boldsymbol{x}_1)\mathcal{Y}_1(\boldsymbol{x}_2)]_0\chi_0(1,2)]_{00}\eta_{11}(1,2), \\ \Phi_1 &= \mathcal{N}_1 e^{-\frac{1}{2}a_1(\boldsymbol{x}_1^2+\boldsymbol{x}_2^2)} \\ &\quad \times [[\mathcal{Y}_1(\boldsymbol{x}_1)\mathcal{Y}_1(\boldsymbol{x}_2)]_1\chi_1(1,2)]_{00}\eta_{11}(1,2), \end{aligned} \quad (11)$$

where $\mathcal{N}_0$ and $\mathcal{N}_1$ are respective normalization constants. Here the shell model is extended to allow for different size parameters, a_0 and a_1, for both the components.

The T-type coordinate $\tilde{\boldsymbol{\rho}} = (\boldsymbol{r}, \boldsymbol{R})$ is also convenient to impose the exchange symmetry for the two nucleons as P_{12} simply changes $\boldsymbol{r} \to -\boldsymbol{r}$ in the orbital function. (For a system consisting of more than three particles, the symmetry requirement will be performed more easily in the V-type coordinate than other Jacobi coordinate sets.) Another set of coordinates commonly used is $\tilde{\boldsymbol{\zeta}} = (\boldsymbol{\zeta}_1, \boldsymbol{\zeta}_2)$, called Y-type, which is related to the V-type coordinate by $\boldsymbol{\zeta}_1 = \boldsymbol{x}_1$ and $\boldsymbol{\zeta}_2 = \boldsymbol{x}_2 - \frac{1}{A_c+1}\boldsymbol{x}_1$, where A_c is the mass number of the core nucleus ($A_c = 4$ in the present case). Each type of coordinate sets emphasizes its characteristic motion. As mentioned above, the V-type is suited for describing the s.p. like motion around the core nucleus [23], whereas the T-type coordinate is suitable for describing the motion corresponding to $\alpha + (2N)$ cluster decomposition. The Y-type coordinate plays a role similar to the V-type. In the limit of large A_c, both the Y- and V-type coordinates coincide.

It should be noted that the basis functions, Eqs. (4) and (7), maintain their functional form under the transformation of the coordinates. The transformation from $\boldsymbol{x}$ to $\boldsymbol{\zeta}$, e.g., is done by a 2×2 matrix T as $\boldsymbol{x} = T\boldsymbol{\zeta}$. Then, it is easy to see that the basis functions change as follows:

$$\begin{aligned} \Psi_{JM}(\Lambda, A, u, \boldsymbol{x}) &= \Psi_{JM}(\Lambda, \tilde{T}AT, \tilde{T}u, \boldsymbol{\zeta}), \\ \Psi_{JM}(\Lambda = (1S), A, \boldsymbol{x}) &= \det T\,\Psi_{JM}(\Lambda = (1S), \tilde{T}AT, \boldsymbol{\zeta}). \end{aligned} \quad (12)$$

This flexibility of the basis function enables one to take account of possible important correlations of the system, just by choosing the nonlinear parameters suitably in only one particular coordinate set.

Owing to the transformation property of Eq. (12), the evaluation of the matrix element of an operator may be made in any convenient set of the coordinates. However, there is one exception. The matrix element for an angular

momentum-dependent operator such as the spin-orbit potential of U_i and the pseudo potential (10), if calculated in the V-type coordinate, contains some error [24], and it should be evaluated in the Y-type Jacobi coordinate set $\boldsymbol{\zeta}$. If the mass number of the core nucleus A_c is sufficiently large as in our previous cases [25], $\boldsymbol{\zeta}_2$ is very well approximated by $\boldsymbol{x}_2$, and the error becomes small. In the present case, however, A_c is only 4, and we will see in Sec. III A that the error is significant.

D. Charge and matter radii

The charge radii of ^{6}He and ^{6}Li can be calculated by taking into account the charge radii of the constituent particles of α and N. As explained in Appendix A, they are calculated from the following formulas

$$r_c^2(^6\mathrm{He}) = \frac{1}{9}\langle \boldsymbol{R}^2\rangle + r_c^2(\alpha) + r_c^2(n), \tag{13}$$

$$r_c^2(^6\mathrm{Li}) = \frac{2}{9}\langle \boldsymbol{R}^2\rangle + \frac{1}{12}\langle \boldsymbol{r}^2\rangle + \frac{2}{3}r_c^2(\alpha) + \frac{1}{3}r_c^2(n) + \frac{1}{3}r_c^2(p)\,. \tag{14}$$

The charge radii of the constituent particles are $\sqrt{r_c^2(\alpha)} = 1.671$ fm [26], $\sqrt{r_c^2(p)} = 0.875$ fm, and $r_c^2(n) = -0.1161\mathrm{fm}^2$ [27]. Equation (13) enables one to deduce model-independent information on the $\langle \boldsymbol{R}^2\rangle$ value from the experimental charge radius of ^{6}He. This will be discussed later. We can extend Eq. (13) to a core $+ n + n$ system:

$$r_c^2(\mathrm{core}+n+n) = \left(\frac{2}{A}\right)^2 \langle \boldsymbol{R}^2\rangle + r_c^2(\mathrm{core}) + \frac{2}{Z}r_c^2(n), \tag{15}$$

where A is the mass number of the system. In a ^{9}Li$+n+n$ three-body model for ^{11}Li, the recent data on the charge radii of ^{9,11}Li [28,29] allow us to deduce $\sqrt{\langle \boldsymbol{R}^2\rangle} = 5.95(3)$ fm.

It is also interesting to calculate the point matter radius which is defined by an rms radius for the point nucleon distribution. The point matter radii of ^{6}He and ^{6}Li are calculated by

$$r_m^2(^6\mathrm{He}, {}^6\mathrm{Li}) = \frac{2}{9}\langle \boldsymbol{R}^2\rangle + \frac{1}{12}\langle \boldsymbol{r}^2\rangle + \frac{2}{3}r_m^2(\alpha), \tag{16}$$

where $r_m^2(\alpha)$ is the mean square matter radius of the α particle and its value can be given by $r_m^2(\alpha) = r_c^2(\alpha) - r_c^2(p) - r_c^2(n)$ under the isospin symmetry that the protons and the neutrons in the α particle have the same mean square radius. In what follows we use $\sqrt{r_m^2(\alpha)} = 1.464$ fm. Using Eqs. (14) and (16) enables us to relate the matter radius of ^{6}Li to its charge radius:

$$r_m^2(^6\mathrm{Li}) = r_c^2(^6\mathrm{Li}) - r_c^2(n) - r_c^2(p)\,. \tag{17}$$

The matter radius of ^{6}Li is thus expressed by only measurable quantities.

E. Electric quadrupole moment

The electric quadrupole moment operator is

$$\hat{Q} = \sqrt{\frac{16\pi}{5}}\sum_i^A e_i \mathcal{Y}_{20}(\boldsymbol{r}_i - \boldsymbol{X}), \tag{18}$$

where e_i is the nucleon charge and $\boldsymbol{X}$ is the center of mass coordinate of the system. This operator can be simplified, in the $\alpha + n + p$ model of ^{6}Li, to

$$\hat{Q} = \hat{Q}_{\boldsymbol{r}} + \hat{Q}_{\boldsymbol{R}} = \sqrt{\frac{16\pi}{5}}e\left\{\frac{1}{4}\mathcal{Y}_{20}(\boldsymbol{r}) + \frac{2}{3}\mathcal{Y}_{20}(\boldsymbol{R})\right\}. \tag{19}$$

Here use is made of the fact that the α particle has spin zero and the two valence nucleons have good isospin. The operator $\hat{Q}_{\boldsymbol{r}}$ is the same as the quadrupole moment operator for the deuteron, while the second term $\hat{Q}_{\boldsymbol{R}}$ corresponds to the quadrupole moment operator for the relative motion between the α particle and the center of mass of the np system.

F. Two-nucleon correlation function

We define the two-nucleon correlation function by

$$\rho(\boldsymbol{x}_1, \boldsymbol{x}_2) = \frac{1}{2J+1}\sum_M \langle \Psi_{JM}|\boldsymbol{x}_1\boldsymbol{x}_2\rangle\langle \boldsymbol{x}_1\boldsymbol{x}_2|\Psi_{JM}\rangle_{\mathrm{ST}}\,. \tag{20}$$

Here $\langle\ldots\rangle_{\mathrm{ST}}$ indicates that the integration is to be performed over the spin and isospin coordinates. Because of the average procedure over the Z component of the total angular momentum, the two-nucleon correlation function becomes scalar, that is, it is a function of x_1, x_2 and θ, the angle between $\boldsymbol{x}_1$ and $\boldsymbol{x}_2$; $\rho(\boldsymbol{x}_1, \boldsymbol{x}_2) = \rho(x_1, x_2, \theta)$. The normalization of the total wave function Ψ_{JM} is expressed as $\iiint \rho(x_1, x_2, \theta) 8\pi^2 x_1^2 x_2^2 \sin\theta dx_1 dx_2 d\theta = 1$.

G. Momentum distribution

The momentum and spatial density distributions of a quantum-mechanical system are obtained through the Wigner phase-space distribution function [8]. The Wigner function is concisely expressed in terms of the density matrix. Since we are interested in the momentum distribution for the relative motion between the valence nucleons, we introduce the density matrix with respect to the relative distance vector $\boldsymbol{r}$, one of the T-type coordinates:

$$\varrho(\boldsymbol{r}, \boldsymbol{r}') = \frac{1}{2J+1}\sum_M \int \langle \Psi_{JM}|\boldsymbol{r}'\boldsymbol{R}\rangle\langle \boldsymbol{r}\boldsymbol{R}|\Psi_{JM}\rangle_{\mathrm{ST}} d\boldsymbol{R}, \tag{21}$$

where $\langle \boldsymbol{r}\boldsymbol{R}|\Psi_{JM}\rangle$ is obtained from $\langle \boldsymbol{x}_1\boldsymbol{x}_2|\Psi_{JM}\rangle$ through the replacement (12) with

$$T = \begin{pmatrix} \frac{1}{2} & 1 \\ -\frac{1}{2} & 1 \end{pmatrix}.$$

We define the density matrix by taking the average over the Z component of the total angular momentum.

The Wigner distribution function is defined through the density matrix as

$$W(\boldsymbol{r}, \boldsymbol{k}) = \frac{1}{(2\pi)^3}\int \varrho\left(\boldsymbol{r} + \frac{\boldsymbol{s}}{2}, \boldsymbol{r} - \frac{\boldsymbol{s}}{2}\right) \mathrm{e}^{i\boldsymbol{k}\cdot\boldsymbol{s}} d\boldsymbol{s}\,. \tag{22}$$

The density distribution for the N-N relative motion is given by the diagonal element of the density matrix

$$\rho(\boldsymbol{r}) = \varrho(\boldsymbol{r}, \boldsymbol{r}) = \int W(\boldsymbol{r}, \boldsymbol{k}) d\boldsymbol{k}, \tag{23}$$

and the momentum distribution for the N-N relative motion is obtained by

$$\rho(\boldsymbol{k}) = \int W(\boldsymbol{r}, \boldsymbol{k}) d\boldsymbol{r} \,. \tag{24}$$

These distributions are normalized as $\int \rho(\boldsymbol{r}) d\boldsymbol{r} = 1$, and $\int \rho(\boldsymbol{k}) d\boldsymbol{k} = 1$. A formula to calculate the density matrix and the momentum distribution is given in Appendix.

III. RESULTS AND DISCUSSIONS

The input parameters we use are $\hbar^2/m_N = 41.47$ MeV fm^2, $m_\alpha = 4m_N$, and $e^2 = 1.440$ MeV fm, where m_N and m_α are the masses of the nucleon and the α particle, respectively. The u parameter of the MN potential is set to $u = 1$. No spin-orbit component of the MN potential is included.

A. Spectroscopic properties

In a single channel calculation with a specific $\Lambda = (LS)$, neither (00) nor (11) channel produces a bound state of ^{6}He below the $\alpha + N + N$ threshold. The case of ^{6}Li is different, depending on the N-N potential. When using the MN potential, the $\Lambda = (01)$ channel gives a bound state, whereas in the case of the G3RS potential no single-channel calculation produces a bound state below the three-body threshold. This difference between the two potential models is due to the tensor force that plays no role in the single (01) channel but gains energy through the coupling with different channels. This mechanism is similar to binding the neutron and the proton in the deuteron with the realistic force.

Full calculations which couple all possible Λ channels of Eq. (8) give the results listed in Table I. The calculation has been performed in the Y-type coordinates. The basis dimension K is 400 for ^{6}He and for ^{6}Li with the MN potential, whereas it is increased to 600 for ^{6}Li with the G3RS potential. The ground states of ^{6}He and ^{6}Li obtained with the G3RS potential are both underbound by 400–500 keV, whereas the MN potential underbinds ^{6}He by more than 500 keV but overbinds ^{6}Li by 200 keV. The underbinding of ^{6}He with the MN potential is partly due to the fact that the ^{1}S$_0$ potential is too repulsive to reproduce the experimental ^{1}S$_0$ phase shifts. The common lack of the binding energies in the case of the G3RS potential can be explained by at least three effects: One is the deficiency of the attraction in the D and F waves of the KKNN potential as discussed in Refs. [14,32]. According to the latter the energy gain of ^{6}He that is obtained by correcting the potential strength is, however, only a few tens of keV. Next is the effect of three-body forces [33] though a conclusive statement on their magnitude remains open. The third effect to be considered is the distortion of the α core to $3N + N$ partition or the clustering of the $A = 6$ nuclei into ^{3}H+^{3}H (for ^{6}He) and ^{3}H+^{3}He (for ^{6}Li). The coupling of the $\alpha + N + N$ three-body configuration to the distorted configuration produces some energy gain. A recent microscopic calculation indicates that the two configurations actually have rather large overlap and that the energy gain is of order of few hundreds keV in ^{6}He [34].

We here remark on the accuracy of the present calculation by comparing to other calculations. For ^{6}He calculated with

TABLE I. Properties of the ground states of ^{6}He and ^{6}Li. Energy and length are given in MeV and fm. The $\boldsymbol{L}^2$ and quadratic $\boldsymbol{L} \cdot \boldsymbol{S}$ terms of the G3RS potential are neglected. See text for the MMN potential. The Coulomb potential is included in the term $\langle U_1^{\rm C} + U_2^{\rm C} \rangle$. Experimental data: $E = -0.975$, $\sqrt{r_c^2} = 2.054(14)$ [30] for ^{6}He; $E = -3.70$, $\sqrt{r_c^2} = 2.55(4)$ [31] or 2.540(30) [29], $\sqrt{r_m^2} = 2.42(4)$ for ^{6}Li.

	^{6}He (0^+)			^{6}Li (1^+)		d (1^+)	
	MN	MMN	G3RS	MN	G3RS	MN	G3RS
E	−0.421	−0.975	−0.460	−3.91	−3.31	−2.20	−2.28
$\langle T_{\boldsymbol{r}} \rangle$	10.87	11.87	12.51	17.56	23.28	10.48	16.48
$\langle v_{12}^{\rm C} \rangle$	−3.77	−4.86	−5.62	−13.41	−7.71	−12.69	−7.29
$\langle v_{12}^{\rm T} \rangle$	—	—	0.107	—	−12.25	—	−11.46
$\langle v_{12}^{\rm LS} \rangle$	—	—	0.021	—	—	—	—
$\langle T_{\boldsymbol{R}} \rangle$	12.47	13.06	12.55	13.29	11.49	—	—
$\langle U_1^{\rm C} + U_2^{\rm C} \rangle$	−17.54	−18.51	−17.71	−19.00	−16.44	—	—
$\langle U_1^{\rm LS} + U_2^{\rm LS} \rangle$	−2.46	−2.54	−2.32	−2.34	−1.69	—	—
$\sqrt{\langle \boldsymbol{r}^2 \rangle}$	5.05	4.63	4.86	3.48	3.58	3.90	3.96
$\sqrt{\langle \boldsymbol{R}^2 \rangle}$	3.89	3.66	3.78	3.49	3.81	—	—
$\sqrt{r_m^2}$	2.63	2.49	2.56	2.27	2.39	—	—
$\sqrt{r_c^2}$	2.09	2.04	2.07	2.41	2.52	—	—
$P(00)$	84.7	86.4	87.5	—	—	—	—
$P(11)$	15.3	13.6	12.5	1.1	0.8	—	—
$P(10)$	—	—	—	6.2	3.9	—	—
$P(01)$	—	—	—	91.7	90.3	100	95.2
$P(21)$	—	—	—	1.0	5.0	—	4.8

the MN potential, our ground state energy, −0.421 MeV, is in excellent agreement with the value −0.42 MeV obtained by the hyperspherical coordinate method [35]. If the calculation is done in the V-type coordinates (which is not correct as mentioned in Sec. II C), the ground-state energy of ^{6}He would go down to −0.749 MeV; the result is again consistent with the values obtained by a Lagrange-mesh calculation [24] and a hybrid T + V model calculation [14]. The corresponding energy for the ^{6}Li ground state would be −4.68 MeV, instead of −3.91 MeV calculated correctly in the Y-type coordinates. These results clearly show that the correct treatment of the coordinates is important in such light systems as ^{6}He and ^{6}Li.

Table I lists the decomposition of the energy into the expectation values of the various pieces of the Hamiltonian, the radii and the probability $P(LS)$ (in a percentage) of finding the $\Lambda = (LS)$ component. Let $E_{\boldsymbol{r}}$ and $E_{\boldsymbol{R}}$ denote, respectively, the energy for the relative motion of the two nucleons and the energy for the relative motion between the α particle and the center-of-mass of the two nucleons. They are defined by

$$\begin{aligned} E_{\boldsymbol{r}} &= \langle T_{\boldsymbol{r}} \rangle + \langle v_{12}^{\mathrm{C}} \rangle + \langle v_{12}^{\mathrm{T}} \rangle + \langle v_{12}^{\mathrm{LS}} \rangle, \\ E_{\boldsymbol{R}} &= \langle T_{\boldsymbol{R}} \rangle + \langle U_1^{\mathrm{C}} + U_2^{\mathrm{C}} \rangle + \langle U_1^{\mathrm{LS}} + U_2^{\mathrm{LS}} \rangle . \end{aligned} \tag{25}$$

In the case of ^{6}He, the G3RS and MN potentials give very similar results for these energies: $(E_{\boldsymbol{r}}, E_{\boldsymbol{R}}) = (7.03, -7.49)$ MeV for G3RS and (7.10, −7.52) MeV for MN. Even each of the expectation values is close to each other as well. The tensor and spin-orbit forces between the two neutrons play a minor role. In contrast to ^{6}He, both the potentials exhibit quite different features in binding ^{6}Li. The partial energies are $(E_{\boldsymbol{r}}, E_{\boldsymbol{R}}) = (3.32, -6.63)$ MeV for G3RS and (4.14, −8.05) MeV for MN, so that the difference between the two is modest. However, the content of $E_{\boldsymbol{r}}$ in particular is quite different between them because of the tensor force and the short-ranged repulsion. In G3RS the large positive value of $\langle T_{\boldsymbol{r}} \rangle$ is balanced by the tensor contribution $\langle v_{12}^{\mathrm{T}} \rangle$. Though this is similar to the case of the deuteron, we see from the values of $\langle T_{\boldsymbol{r}} \rangle$ and $\sqrt{\langle \boldsymbol{r}^2 \rangle}$ that the *np* pair in ^{6}Li is more compressed than the one in the deuteron. In spite of these differences the $P(LS)$ values of ^{6}Li are rather similar in the two potentials except for the $(LS) = (21)$ channel, which is largely determined through the tensor coupling to the dominating channel of $(LS) = (01)$. As will be discussed later, the ^{6}Li quadrupole moment is very sensitive to this coupling. The spin-triplet channels occupy about 95%.

The ^{6}Li charge radius calculated using the G3RS potential agrees with the experimental value determined from the electron scattering [31] and the isotope shift in lithium [29], but the MN potential gives the charge radius, which is small by at least 0.1 fm. This failure of the MN potential is due to that the $\sqrt{\langle \boldsymbol{R}^2 \rangle}$ value is predicted to be too small. As Eq. (17) shows, the use of the ^{6}Li charge radius leads to an "experimental" rms matter radius $\sqrt{r_m^2(^6\mathrm{Li})} = 2.42(4)$ fm, which is consistent with that determined from the analysis of proton elastic scatterings at intermediate energies, $\sqrt{r_m^2(^6\mathrm{Li})} = 2.45(7)$ fm [36,37]. The theoretical value calculated with the G3RS potential is 2.39 fm, in agreement with experiment.

Now we turn to the case of ^{6}He. The charge radius of ^{6}He has recently been measured by laser spectroscopy technique [30]. Our theoretical value agrees fairly well with the experimental value. Using the observed charge radius of ^{6}He in Eq. (13), we can deduce the "experimental" value of $\sqrt{\langle \boldsymbol{R}^2 \rangle}$, which turns out to be 3.726(69) fm. Our value of 3.78 fm is very consistent with this value considering the fact that the calculated binding energy is small by 500 keV. The rms matter radius of ^{6}He extracted from the proton elastic scattering is $\sqrt{r_m^2(^6\mathrm{He})} = 2.30(7)$ fm [37], which is, however, smaller than the value (2.48 ± 0.03 fm) deduced from the interaction cross-section analysis [38]. The theory with the G3RS or MN potential predicts too large matter radius for ^{6}He; this overestimation is related to that the calculated binding energy is too small, leading to a too large value for $\sqrt{\langle \boldsymbol{r}^2 \rangle}$. Because the attraction of the MN potential is weak in the $^1S_0$ channel, we repeated the calculation by increasing the strength of its longest range part from −91.85 to −91.85 × 1.07 MeV so as to reproduce the binding energy. This potential is called MMN, and its result is listed in Table I. As expected, the rms matter radius now decreases from 2.63 to 2.49 fm, which is consistent with the values of the interaction cross-section measurement as well as the fully microscopic three-cluster calculations [18,34].

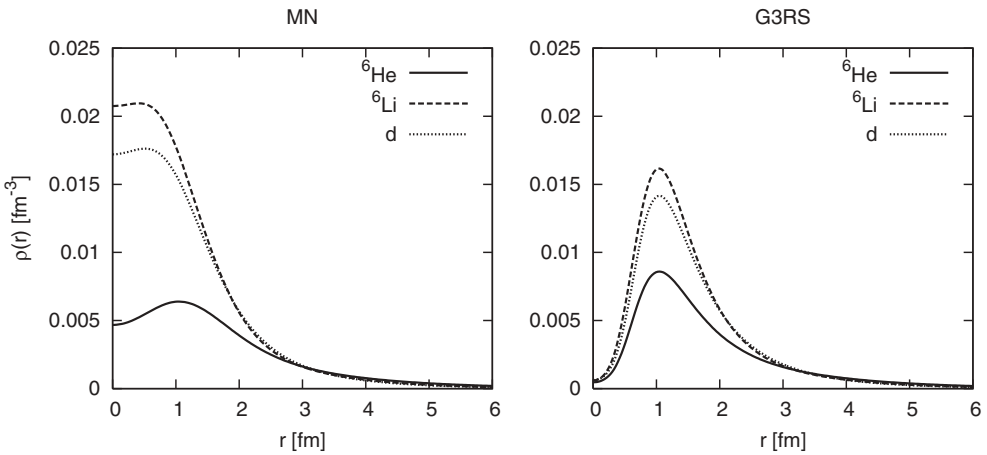

FIG. 1. Density distributions, calculated from the G3RS and MN potentials, of the two-nucleon relative motion in ^{6}He, ^{6}Li, and the deuteron.

TABLE II. Electric quadrupole moments of ^{6}Li and the deuteron in e fm^2. Values in the parentheses are the contributions of the cross terms between the $(LS) = (01)$ and $(LS) = (21)$ components of the ^{6}Li ground-state wave function. The experimental values are $-0.08178(164)$ e fm^2 [39] for ^{6}Li and $0.2860(15)e$ fm^2 [40] for the deuteron.

	^{6}Li (1^+)		d (1^+)
	MN	G3RS	G3RS
Q	-0.295	0.164	0.264
	(-0.396)	(0.088)	
Q_r	-0.034	0.198	0.264
	(-0.094)	(0.160)	
Q_R	-0.260	-0.034	—
	(-0.302)	(-0.072)	

The electric quadrupole moment of ^{6}Li is a long-standing problem. The ^{6}Li quadrupole moment is negative and small, $-0.08178(164)$ e fm^2 [39], whereas the deuteron quadrupole moment is $0.2860(15)$ e fm^2 [40]. Thus it is known that the $\alpha + n + p$ model which assumes $(0s)^4$ α-cluster gives the wrong sign even when the tensor force is included [6]. See also Ref. [41]. Though we do not attempt to solve this enigmatic issue, we just show the result of the present model in Table II. As expected, the ^{6}Li quadrupole moment obtained with the G3RS potential turns out to be positive (0.164 e fm^2). Interestingly, the quadrupole moment with the MN potential becomes -0.295 e fm^2; this happens because the large negative contribution of Q_R is not canceled by the Q_r value. This contrast between the two potential models is mainly due to the different contribution of the cross terms between the $(LS) = (01)$ and $(LS) = (21)$ components of the ^{6}Li ground-state wave function. See the parenthetic values in Table II. The mixing of these components is due to the tensor force. Therefore the failure of the ^{6}Li quadrupole moment indicates that we have to consider the effect of the tensor force between the core and the valence nucleons. It should be noted that a variational Monte Carlo calculation gives the quadrupole moment of $-0.23(9)$ e fm^2 [42].

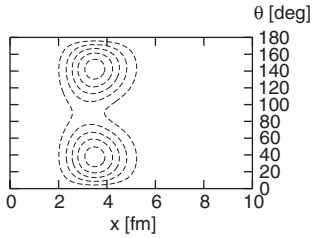

FIG. 2. Contour map of the two-nucleon correlation function, $8\pi^2 x^4 \sin\theta\rho(x, x, \theta)$, calculated from the uncorrelated p-shell wave function, Eq. (26). The difference between any two neighboring contour levels is 0.01 fm^{-2}.

B. Two-nucleon correlation function

Figure 1 plots the density distributions $\rho(\boldsymbol{r})$ (normalized to unity) of the two-nucleon relative motion in ^{6}He, ^{6}Li, and the deuteron. The densities calculated using the G3RS potential (right panel) show central dips due to the short-ranged repulsion, but beyond $r = 1.5$ fm they are similar to those calculated with the MN potential (left panel). The density of

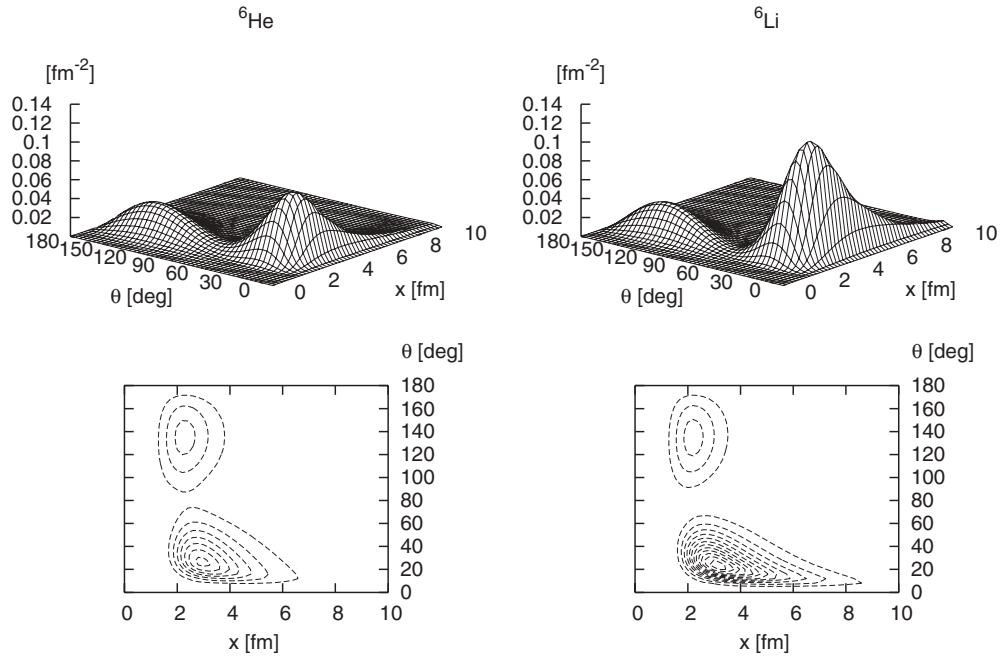

FIG. 3. Two-nucleon correlation functions, $8\pi^2 x^4 \sin\theta\rho(x, x, \theta)$, calculated with the G3RS potential for ^{6}He and ^{6}Li. The lower panels are their contour maps, and the difference between any two neighboring contour levels is 0.01 fm^{-2}.

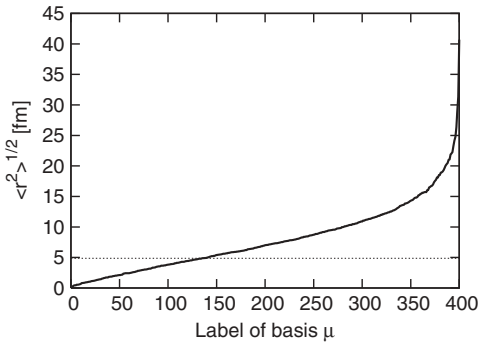

FIG. 4. Eigenvalues of the rms distance between the two neutrons, $\sqrt{\langle \boldsymbol{r}^2 \rangle}$, calculated from the basis functions for ^{6}He. The G3RS potential is used. Dotted line denotes the rms distance (4.86 fm) of ^{6}He.

^{6}He reaches furthest in the distance, and as a result its density around $r = 1 \sim 2$ fm is considerably smaller than that of ^{6}Li. Comparing the densities between ^{6}Li and the deuteron, we see that the *np* relative motion in ^{6}Li shrinks compared to that of the deuteron (see also the $\sqrt{\langle \boldsymbol{r}^2 \rangle}$ value in Table I).

The correlated motion of the valence nucleons reflects on the two-nucleon correlation function $\rho(x_1, x_2, \theta)$. Before discussing the correlated motion, we first examine the function $\rho(x_1, x_2, \theta)$ that is generated from an "uncorrelated" basis function Φ for ^{6}He. For this purpose we take a combination of the two p-shell harmonic-oscillator functions (11),

$$\Phi = \sqrt{1 - C^2}\Phi_0 + C\Phi_1, \tag{26}$$

and determine (a_0, a_1, C) so as to maximize the overlap, $|\langle \Phi | \Psi_{00} \rangle|^2$, with the ^{6}He ground-state wave function Ψ_{00} obtained using the G3RS potential. The resulting values are $a_0 = 0.163$ fm^{-2}, $a_1 = 0.194$ fm^{-2}, and $C = 0.402$, leading to $|\langle \Phi | \Psi_{00} \rangle|^2 = 0.75$. The simple wave function Φ has a surprisingly large overlap with the realistic wave function Ψ_{00}. Though the overlap is fairly large, Φ includes no correlated configurations and indeed the energy calculated with Φ is high (8.77 MeV). The two-nucleon correlation function $\rho(x_1, x_2, \theta)$ calculated from Φ becomes a function of $\cos^2\theta$, so that $\rho(x, x, \theta)$ multiplied by $8\pi^2 x^4 \sin\theta$ is symmetric with respect to $\theta = 90^\circ$. See Fig. 2. An asymmetry with respect to $\theta = 90^\circ$ would indicate the presence of correlation in the $A = 6$ nuclei.

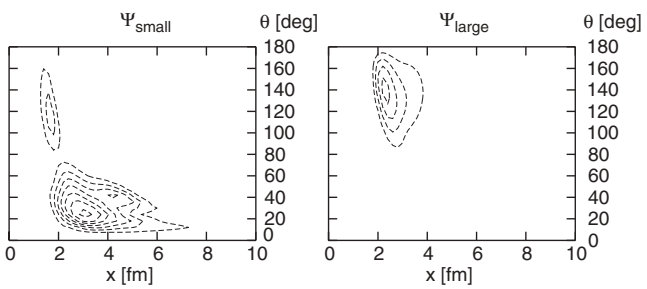

FIG. 5. Decomposition of the two-nucleon correlation function of ^{6}He into the small (left panel) and large (right panel) components. The G3RS potential is used. The difference between any two neighboring contour levels is 0.01 fm^{-2}.

Now let us discuss the two-nucleon correlation function that derives from the dynamical calculation with the G3RS potential. The MN potential gives similar two-nucleon correlation function. Figure 3 displays the contour maps of $8\pi^2 x^4 \sin\theta \rho(x, x, \theta)$ for ^{6}He and ^{6}Li. In both the cases we clearly see asymmetric patterns with two distinct peaks: In ^{6}He the highest peak is located at $(x, \theta) = (2.9, 26^\circ)$ with a height of 0.07 fm^{-2}, whereas in ^{6}Li the highest peak is located at $(x, \theta) = (3.2, 24^\circ)$ with a height of 0.13 fm^{-2}. Here x is given in fm. The peak in ^{6}Li called the deuteron-like correlation is about twice higher than that called the dineutron-like correlation in ^{6}He. Comparing Fig. 3 with Fig. 2, we learn that the two-nucleon interaction enhances the asymmetric pattern. Another lower peak that shows up at larger angles is called a cigarlike correlation. It corresponds to the geometry that the two nucleons sit on the opposite sides of the core. This type of peak is located at $(x, \theta) = (2.3, 136^\circ)$ for ^{6}He and at $(x, \theta) = (2.4, 136^\circ)$ for ^{6}Li, respectively. Their heights are both 0.03 fm^{-2}, which is about half of the peak height in Fig. 2.

C. Projection to dineutron- and cigarlike configurations

In Sec. III B we discussed the two-nucleon correlated motion from the viewpoint of the asymmetric appearance of the dineutron- and cigarlike peaks. Here we ask a question of how the two peaks appear in relation to the density or rms distance distribution of the two nucleons. We expect that the dineutron-like peak in ^{6}He is formed from those components of the wave function that have smaller rms distance, whereas the cigarlike peak is constructed from the rest of the components.

As Eq. (3) shows, the wave function is given as a combination of K nonorthogonal basis functions. By taking a suitable linear transformation of these K bases, we can obtain an orthonormal set $\Xi_{JM}(\mu)$,

$$\Xi_{JM}(\mu) = \sum_{i=1}^{K} W_{\mu i} \Psi_{JM}(\Lambda_i, A_i, u_i), \tag{27}$$

with the condition $\langle \Xi_{JM}(\mu) | \Xi_{JM}(\mu') \rangle = \delta_{\mu,\mu'}$. It is convenient for the present purpose to choose the coefficients $W_{\mu i}$ in such a way that they diagonalize the squared distance $\boldsymbol{r}^2$ between the two nucleons, that is,

$$\langle \Xi_{JM}(\mu) | \boldsymbol{r}^2 | \Xi_{JM}(\mu') \rangle = \langle \boldsymbol{r}^2 \rangle_\mu \delta_{\mu,\mu'} . \tag{28}$$

By arranging the eigenvalues $\langle \boldsymbol{r}^2 \rangle_\mu$ in increasing order ($\mu = 1, 2, \ldots, K$), we display in Fig. 4 the distribution of the rms distance in the case of ^{6}He, where $K = 400$ and the minimum and maximum eigenvalues of $\sqrt{\langle \boldsymbol{r}^2 \rangle_\mu}$ are 0.223 and 40.7 fm, respectively. The fact that the eigenvalues cover the wide region from small to large distances indicates that the SVM basis selection is efficiently performed to take into account the short-ranged correlation as well as the asymptotic behavior. We can see that the basis states $\Xi_{JM}(\mu)$ of the first 320 members give rather uniform distribution of $\sqrt{\langle \boldsymbol{r}^2 \rangle_\mu}$ up to about 12 fm, whereas the rest of the basis states cover the eigenvalues of larger rms distances.

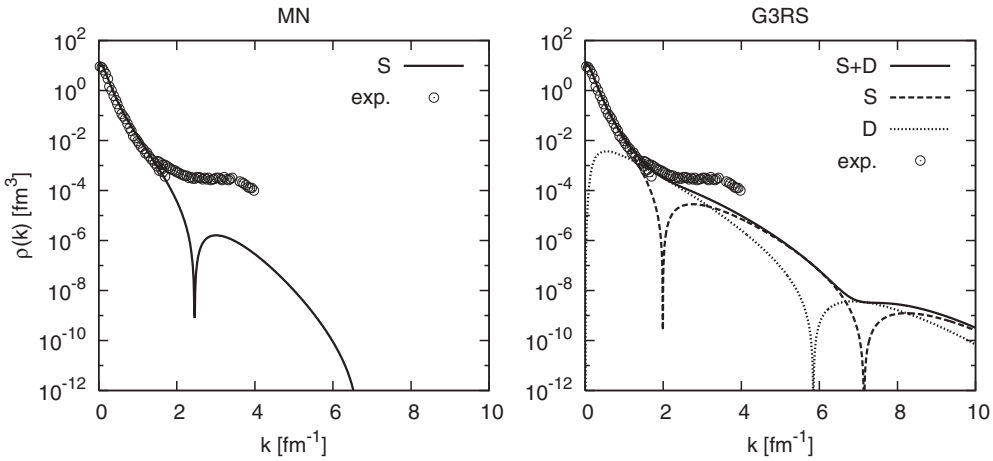

FIG. 6. Momentum distributions of the deuteron calculated with the G3RS and MN potentials. Experimental data are taken from Ref. [44].

We define two projectors that are orthogonal complements to each other:

$$P_{\text{small}} = \sum_{\mu=1}^{\kappa} |\Xi_{JM}(\mu)\rangle\langle\Xi_{JM}(\mu)|,$$
$$P_{\text{large}} = \sum_{\mu=\kappa+1}^{K} |\Xi_{JM}(\mu)\rangle\langle\Xi_{JM}(\mu)|, \tag{29}$$

with $P_{\text{small}} + P_{\text{large}} = 1$. The projector P_{small} projects into the subspace spanned by those $\Xi_{JM}(\mu)$ that have smaller $\langle \boldsymbol{r}^2\rangle_\mu$ values, whereas P_{large} is the projector into the rest that is spanned by the basis states with larger rms values. The total wave function is decomposed into two orthogonal components, "small" and "large," using the projectors

$$\Psi_{JM} = P_{\text{small}}\Psi_{JM} + P_{\text{large}}\Psi_{JM} \equiv \Psi_{\text{small}} + \Psi_{\text{large}}\,. \tag{30}$$

For the sake of simplicity, we choose κ in Eq. (29) such that $|\langle\Psi_{\text{small}}|\Psi_{JM}\rangle|^2$ is as close as to 0.5. It turns out that $\kappa = 88$ and the corresponding rms eigenvalue is $\sqrt{\langle \boldsymbol{r}^2\rangle_\kappa} = 3.47$ fm.

It is now possible to decompose the expectation value of an operator $\mathcal{O}$ into three terms, that is, small and large and their interference terms:

$$\langle\Psi_{JM}|\mathcal{O}|\Psi_{JM}\rangle = \langle\Psi_{\text{small}}|\mathcal{O}|\Psi_{\text{small}}\rangle + \langle\Psi_{\text{large}}|\mathcal{O}|\Psi_{\text{large}}\rangle + \{\langle\Psi_{\text{small}}|\mathcal{O}|\Psi_{\text{large}}\rangle + \langle\Psi_{\text{large}}|\mathcal{O}|\Psi_{\text{small}}\rangle\}\,. \tag{31}$$

We apply this decomposition to the two-nucleon correlation function to see how the contour map of ^{6}He (Fig. 3) is constructed. Plotted in Fig. 5 are those contributions to the contour map which are calculated with Ψ_{small} and Ψ_{large}, respectively. The contribution of the interference term is found to be small and can be safely ignored. Comparing this decomposition with the full contour map of ^{6}He in Fig. 3, we can safely conclude that the dineutron-like correlation is generated by the small component Ψ_{small} and the cigarlike correlation by the large component Ψ_{large}.

D. Momentum distribution

Though the contour map discussed in Secs. III B and III C shows some correlation effects, it is not clear how the correlated features in ^{6}He and ^{6}Li are observed experimentally.

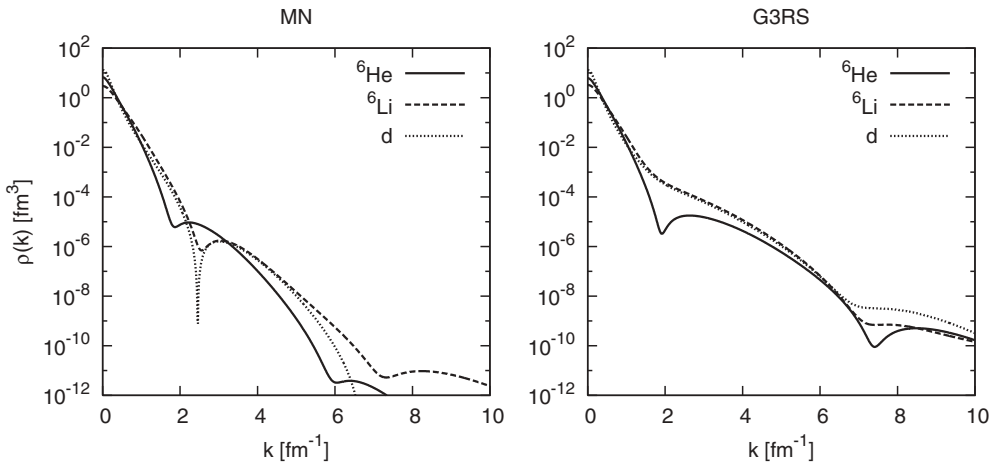

FIG. 7. Momentum distributions, calculated from the G3RS and MN potentials, of the valence nucleons in ^{6}He and ^{6}Li.

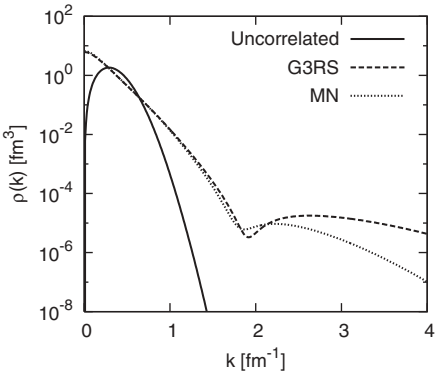

FIG. 8. Momentum distributions of the valence nucleons in ^{6}He for the three different wave functions.

Comparative experiments of the intermediate energy proton elastic scatterings on ^{6}He and ^{6}Li [36,37] have been performed to elucidate the matter densities of both the nuclei, but the analysis of the experimental data is confronted with some ambiguities because the scattering is confined to extremely forward angles. As mentioned in the Introduction, the measurement of the momentum distribution in a special arrangement seems to be accessible in the inverse kinematics, providing data that are sensitive to the different structures of ^{6}He and ^{6}Li.

It is well known that the momentum distribution of the *np* relative motion in the deuteron shows different behavior in the *S*- and *D*-wave contributions. The momentum distribution is calculated from the density matrix of the deuteron as in Eq. (21). As displayed in the right panel of Fig. 6, the *S*-wave contribution to the momentum distribution is peaked at lower momentum and has a dip at $k \sim 2$ fm^{-1}. The *D*-wave component of the deuteron, however, fills the dip. This characteristics of the distribution is supported by experiment [43]. In contrast to this, the momentum distribution (left panel) obtained with the MN potential does show a dip because it has no *D*-wave component, and in addition the momentum distribution decreases quickly with increasing k because the short-ranged repulsion is not as strong as the G3RS potential. To compare with experiment at k higher than 2 fm^{-1}, however, it is important to include meson exchange currents and isobar currents dominated by the Δ excitation. See Ref. [44] and Fig. 6.

The momentum distributions of ^{6}He, ^{6}Li, and the deuteron are compared in Fig. 7 for the G3RS (right panel) and MN (left panel) potentials. The realistic potential of G3RS gives the momentum distributions characterized as follows: The momentum distribution of ^{6}Li is very similar to that of the deuteron, but the momentum distribution of ^{6}He differs from them, showing a clear dip at $k \sim 2$ fm^{-1}. These features are understood from the difference in the partial wave contents of the N-N relative motion; ^{6}Li contains the *D*-wave component as the deuteron does, whereas ^{6}He is dominated by the *S*-wave component. The most distinctive difference between ^{6}He and ^{6}Li appears around $k \sim 2$ fm^{-1}. In this region, however, the momentum distribution becomes by four or more orders of magnitude smaller than that at $k \sim 0$; this may make it hard to measure the cross section experimentally. If the measurement of the momentum distribution is possible in this region, one can learn the role of the tensor force acting between the valence nucleons, provided that the meson exchange currents and the isobar excitations are still not so important.

Figure 8 compares the momentum distributions of ^{6}He corresponding to the three different wave functions, those obtained with G3RS and MN and the uncorrelated one defined in Eq. (26). Both the G3RS and MN distributions are similar up to the dip region. Beyond $k \sim 2$ fm^{-1} the momentum distribution of G3RS surpasses that of MN, which is due to the difference in the short-range correlation involved in the two wave functions. The uncorrelated wave function gives the momentum distribution that is quite different from those of the correlated wave functions even at $k \sim 1$fm^{-1}.

In Sec. III C we decomposed the ground-state wave function of ^{6}He into $\Psi_{\rm small}$ and $\Psi_{\rm large}$, and confirmed that the dineutron-like peak is produced by the small component $\Psi_{\rm small}$, whereas the cigarlike peak by the large component $\Psi_{\rm large}$. The interference term was small. One might expect that the momentum distribution may as well be decomposed into

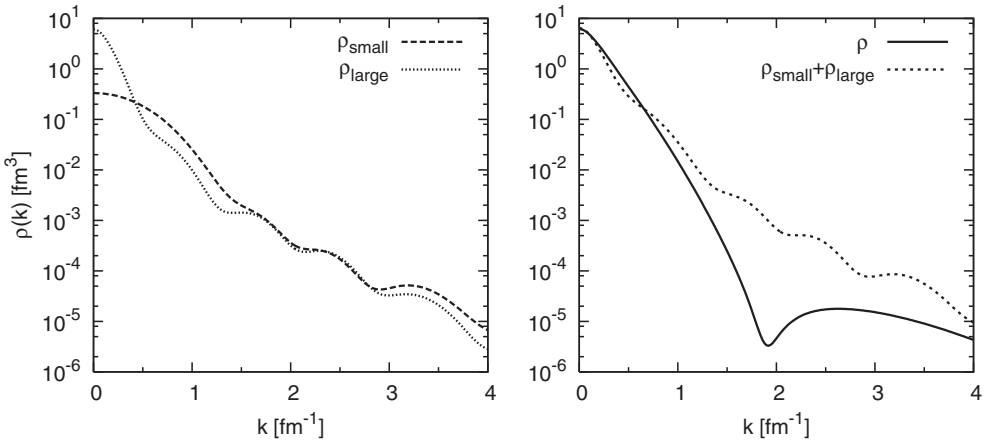

FIG. 9. Momentum distribution of the valence nucleons in ^{6}He and its decomposition into small and large components. See the text for detail. The G3RS potential is used.

low- and high-momentum components. Namely $\Psi_{\rm large}$ may contribute to the momentum distribution at small k, whereas $\Psi_{\rm small}$ to the high-momentum component. We examine this expectation in Fig. 9 by analyzing the momentum distribution of ^{6}He obtained with the G3RS potential. The left panel shows the partial momentum distributions, $\rho_{\rm large}$ calculated with $\Psi_{\rm large}$ and $\rho_{\rm small}$ calculated with $\Psi_{\rm small}$, respectively. The right panel compares the full momentum distribution ρ with the incoherent sum of $\rho_{\rm large} + \rho_{\rm small}$, so that the difference between ρ and $\rho_{\rm large} + \rho_{\rm small}$ is the contribution of the interference terms of Eq. (31). We see that the contribution of the interference terms can be neglected for $k < 1$ fm^{-1}. However, the interference contribution becomes important for $k > 1$ fm^{-1}. In the momentum region where the interference can be ignored, the momentum distribution is dominated by $\Psi_{\rm large}$ for $k < 0.5$ fm^{-1} and by $\Psi_{\rm small}$ for $0.5 < k < 1$ fm^{-1}.

IV. CONCLUSIONS

To study the correlation and the momentum distribution of the two-nucleon relative motion in the ground states of ^{6}He and ^{6}Li, we have described these states in a three-body model of $\alpha + N + N$ where the α particle is assumed to be an inert core. We used a parity-dependent α-N potential that reproduces the low-energy S- and P-wave phase shifts, and two different types of N-N interactions as the potential acting between the two valence nucleons. One is a realistic potential that contains the tensor and spin-orbit forces and the other is an effective potential that includes no tensor component. These were used to compare how much the different N-N potentials affect the correlation and the momentum distribution.

We have obtained the solution of the three-body problem by approximating the ^{6}He and ^{6}Li ground-state wave functions in terms of a combination of explicitly correlated Gaussian basis functions. The use of the global vectors to describe a nonspherical orbital motion facilitates the calculation of the matrix elements much easier than the partial-wave expansion and, moreover, provides us with a solution of high accuracy.

The energies and rms radii of ^{6}He and ^{6}Li are compared to those of experiment. The energies calculated with the realistic N-N potential are underbound by 400–500 keV in both the cases. The charge radii of ^{6}He and ^{6}Li and the matter radius of ^{6}Li are in fair agreement with the observed values. The ^{6}He matter radius is predicted to be larger than those of experiment; the result is due to the underbinding of the calculated ground state of ^{6}He. We have analyzed the two-neutron correlated motion in ^{6}He to identify how the dineutron and cigarlike configurations are related to the two-neutron relative distance distribution.

The momentum distributions of the N-N relative motion have been compared between ^{6}He and ^{6}Li. The distributions obtained with the effective potential show the pattern characteristic of S-wave dominance and fall rapidly as the momentum increases. In the case of the realistic potential, the momentum distribution in ^{6}Li is very similar to that of the deuteron. That is, both the S and D waves contribute to the momentum distribution that monotonically decreases with an increasing momentum. In contrast to this, the ^{6}He momentum distribution is dominated by the S wave, showing a clear dip at $k \sim 2$ fm^{-1}. The most prominent difference in their momentum distributions thus shows up around $k = 2$ fm^{-1}. The difference between ^{6}He and ^{6}Li is primarily due to whether the tensor force plays an important role of mixing the D-state probability between the N-N relative motion. We hope that this prediction will be tested experimentally.

Note added in proof. After the acceptance of this paper, we have found a recent paper by Schiavilla *et al.* entitled "Tensor Forces and the Ground-State Structure of Nuclei" [45]. These authors discuss two-nucleon momentum distributions of the ground states of nuclei with mass number $A \leqslant 8$. They have considered the momentum distributions averaged over all the np or pp pairs in the nuclei, while we have calculated the momentum distribution for the valence nucleons in ^{6}He and ^{6}Li. In spite of these differences, both calculations show similar results concerning the dominance of np distribution over nn (or pp) distribution, particularly in the region of $k = 2\,\text{fm}^{-1}$, and the important role of the tensor force which leads to those characteristics.

ACKNOWLEDGMENTS

The authors thank T. Suda for his interest and valuable discussions. They thank D. Baye for useful discussions on the three-body calculations. W. H. thanks the Japan Society for the Promotion of Science for research support. This work was in part supported by Japan-Belgium Bilateral Joint Research Project of Japan Society for the Promotion of Science and a grant for Promotion of Niigata University Research Projects (2005–2007).

APPENDIX A: CHARGE AND MATTER RADII IN A THREE-BODY MODEL

To calculate the charge radius of the core $+ N + N$ system, we must take into account the charge radii of the constituent particles of the core and N. Let e_p and $r_c^2(p)$ denote the charge (in the unit of e) and the square of the charge radius of the constituent particle, and let ρ_p denote its charge distribution. When this particle is centered at $\boldsymbol{d}$ from the center-of-mass of the three-body system, its contribution to the square of the charge radius is

$$\frac{1}{Z}\int (\boldsymbol{d}+\boldsymbol{s})^2 \rho_p(\boldsymbol{s}) d\boldsymbol{s} = \frac{1}{Z}\{e_p \boldsymbol{d}^2 + [e_p] r_c^2(p)\}, \quad \text{(A1)}$$

where Z is the charge of the three-body system and $[e_p] = e_p$ for $e_p \neq 0$ and $[e_p] = 1$ for $e_p = 0$. Here $\rho_p(\boldsymbol{s})$ is assumed to be a spherically symmetric function. Applying Eq. (A1) to the three-body system we obtain Eqs. (13) and (14) for the charge radii of ^{6}He and ^{6}Li. In the case of the core $+ n + n$ system, the core is centered at $\boldsymbol{d} = -\frac{2}{A}\boldsymbol{R}$ and the two neutrons are at $\boldsymbol{d} = \frac{A-2}{A}\boldsymbol{R} \pm \frac{1}{2}\boldsymbol{r}$. Using these results in Eq. (A1), we obtain the expression (15) for the charge radius of the system.

It is also interesting to calculate the point matter radius that is defined by a rms radius for the point nucleon distribution. This is possible in exactly the same way as the charge radius simply by replacing Eq. (A1) with the following equation

$$\frac{1}{A}\int (\boldsymbol{d}+\boldsymbol{s})^2\rho_p(\boldsymbol{s})d\boldsymbol{s} = \frac{1}{A}\left[A_p\boldsymbol{d}^2 + A_p r_m^2(p)\right], \quad \text{(A2)}$$

where ρ_p now stands for the mass distribution of the constituent particle and where A_p is the mass number of the particle and $r_m^2(p)$ the mean square matter radius of the particle.

APPENDIX B: CALCULATION OF THE MOMENTUM DISTRIBUTION

The aim of this appendix is to show a method of calculating the momentum distribution for the correlated Gaussians. As discussed in Sec. II G, the momentum distribution is calculated from the density matrix, so that it is sufficient to show how the density matrix is evaluated. We first express the basis functions in the T-type coordinates (z_1, z_2) as discussed in Sec. II C (in this appendix we use (z_1, z_2) instead of $(\boldsymbol{r}, \boldsymbol{R})$ to simplify the notation) and write the general form of the orbital part of the correlated Gaussians as

$$G_{LM_L}(A, \ell_1, \ell_2, z_1, z_2) = \exp\left(-\frac{1}{2}\tilde{z}Az\right) \times [\mathcal{Y}_{\ell_1}(z_1)\mathcal{Y}_{\ell_2}(z_2)]_{LM_L}. \quad \text{(B1)}$$

The density matrix ρ that we consider here reads as

$$\rho(z_1, z_1') = \frac{1}{2J+1}\sum_M \langle [G_{L'}(A', \ell_1', \ell_2', z_1', z_2)\chi_{S'}(1,2)]_{JM}| \times |[G_L(A, \ell_1, \ell_2, z_1, z_2)\chi_S(1,2)]_{JM}\rangle, \quad \text{(B2)}$$

where the integration in the matrix element has to be performed for z_2 as well as the spin coordinates.

Performing the integration over the spin coordinates yields

$$\rho(z_1, z_1') = \delta_{LL'}\delta_{SS'}\frac{1}{2L+1}\sum_{M_L}\langle G_{LM_L}(A', \ell_1', \ell_2', z_1', z_2) \times |G_{LM_L}(A, \ell_1, \ell_2, z_1, z_2)\rangle. \quad \text{(B3)}$$

Writing the angular part of the right-hand side of Eq. (B3) explicitly we obtain

$$\frac{1}{2L+1}\sum_{M_L}[\mathcal{Y}_{\ell_1}(z_1)\mathcal{Y}_{\ell_2}(z_2)]_{LM_L}[\mathcal{Y}_{\ell_1'}(z_1')\mathcal{Y}_{\ell_2'}(z_2)]^*_{LM_L} = (-1)^{\ell_1'+\ell_2'}\frac{1}{\sqrt{2L+1}}\sum_\lambda \begin{bmatrix} \ell_1 & \ell_2 & L \\ \ell_1' & \ell_2' & L \\ \lambda & \lambda & 0 \end{bmatrix} C(\ell_2\ell_2';\lambda)z_2^{2n} \times [[\mathcal{Y}_{\ell_1}(z_1)\mathcal{Y}_{\ell_1'}(z_1')]_\lambda \mathcal{Y}_\lambda(z_2)]_{00}, \quad \text{(B4)}$$

where [ ] is the $9j$ symbol in unitary form and C is the coefficient to couple two spherical harmonics with a same argument:

$$C(\ell_2\ell_2';\lambda) = \sqrt{\frac{(2\ell_2+1)(2\ell_2'+1)}{4\pi(2\lambda+1)}}\langle \ell_2 0 \ell_2' 0|\lambda 0\rangle. \quad \text{(B5)}$$

Note that $2n \equiv \ell_2 + \ell_2' - \lambda$ is non-negative and even, otherwise the coefficient $C(\ell_2\ell_2';\lambda)$ vanishes. Thus the integration over z_2 in Eq. (B3) is performed as

$$\int \exp\left(-\frac{1}{2}az_2^2 - \boldsymbol{Z}\cdot z_2\right) z_2^{2n}[[\mathcal{Y}_{\ell_1}(z_1)\mathcal{Y}_{\ell_1'}(z_1')]_\lambda \mathcal{Y}_\lambda(z_2)]_{00}dz_2 = 4\pi(-1)^\lambda[\mathcal{Y}_\lambda(\boldsymbol{Z})[\mathcal{Y}_{\ell_1}(z_1)\mathcal{Y}_{\ell_1'}(z_1')]_\lambda]_{00} \times \sqrt{\frac{\pi}{2}}\frac{(2n)!!}{a^{n+\lambda+\frac{3}{2}}}L_n^{(\lambda+\frac{1}{2})}\left(-\frac{Z^2}{2a}\right)\exp\left(\frac{Z^2}{2a}\right), \quad \text{(B6)}$$

where $L_n^{(\lambda+\frac{1}{2})}$ is the associated Laguerre polynomial, and

$$a = A_{22} + A_{22}', \quad \boldsymbol{Z} = A_{12}z_1 + A_{12}'z_1'. \quad \text{(B7)}$$

By using the formula (6), the coupling of three $\mathcal{Y}$'s in Eq. (B6) reduces to

$$[\mathcal{Y}_\lambda(\boldsymbol{Z})[\mathcal{Y}_{\ell_1}(z_1)\mathcal{Y}_{\ell_1'}(z_1')]_\lambda]_{00} = \sum_k \sqrt{\frac{4\pi(2\lambda+1)!}{(2k+1)!(2\lambda-k+1)!}}A_{12}^k A_{12}'^{\lambda-k} \times \sum_\mu \begin{bmatrix} k & \lambda-k & \lambda \\ \ell_1 & \ell_1' & \lambda \\ \mu & \mu & 0 \end{bmatrix} C(k\ell_1;\mu)C(\lambda-k\ell_1';\mu) \times z_1^{k+\ell_1}z_1'^{\lambda-k+\ell_1'}[Y_\mu(z_1)Y_\mu(z_1')]_{00}, \quad \text{(B8)}$$

with

$$[Y_\mu(z_1)Y_\mu(z_1')]_{00} = (-1)^\mu\frac{\sqrt{2\mu+1}}{4\pi}\sum_{\kappa=0}^{[\frac{\mu}{2}]}(-1)^\kappa \times \frac{(2\mu-2\kappa-1)!!}{(\mu-2\kappa)!(2\kappa)!!}\left(\frac{z_1\cdot z_1'}{z_1z_1'}\right)^{\mu-2\kappa}, \quad \text{(B9)}$$

where $[\frac{\mu}{2}]$ is the largest integer less than or equal to $\frac{\mu}{2}$.

Combining Eqs. (B3)–(B9), we obtain the density matrix as a combination of terms

$$z_1^{2p}z_1'^{2p'}(z_1\cdot z_1')^q\exp\left(-\beta z_1^2 - \beta' z_1'^2 - \gamma z_1\cdot z_1'\right), \quad \text{(B10)}$$

where p, p', and q are all non-negative integers.

To calculate the momentum distribution we just replace (z_1, z_1') with $(\boldsymbol{r}+\frac{1}{2}\boldsymbol{s}, \boldsymbol{r}-\frac{1}{2}\boldsymbol{s})$ in the density matrix, multiply $e^{i\boldsymbol{k}\cdot\boldsymbol{s}}$, and integrate over $\boldsymbol{r}$ and $\boldsymbol{s}$. Renaming $(\boldsymbol{r}, \boldsymbol{s})$ as (z_1, z_2) again, the integration results in the following form

$$\iint e^{-\frac{1}{2}\tilde{z}Bz+i\tilde{k}z}z_1^{2n_1}z_2^{2n_2}(z_1\cdot z_2)^{n_3}dz_1dz_2, \quad \text{(B11)}$$

which can be performed analytically, where B is a 2×2 symmetric matrix, $\tilde{\boldsymbol{k}}\boldsymbol{z} = \boldsymbol{k}\cdot z_1 - \boldsymbol{k}\cdot z_2$ and n_1, n_2, and n_3 are all non-negative integers.

[1] F. M. Marqués *et al*., Phys. Lett. **B476**, 219 (2000).
[2] T. Suda *et al*., private communication.
[3] K. Sekiguchi *et al*., Phys. Rev. C **65**, 034003 (1995).
[4] R. Ent *et al*., Nucl. Phys. **A578**, 93 (1994).
[5] S. Funada, H. Kameyama, and Y. Sakuragi, Nucl. Phys. **A575**, 93 (1994).
[6] A. Csótó and R. G. Lovas, Phys. Rev. C **46**, 576 (1992).
[7] M. V. Zhukov, B. V. Danilin, A. A. Korsheninnikov, and L. V. Chulkov, Nucl. Phys. **A538**, 375c (1992); M. V. Zhukov *et al*., Phys. Rep. **231**, 151 (1993).
[8] E. Wigner, Phys. Rev. **40**, 749 (1932).
[9] J. Hüfner and M. C. Nemes, Phys. Rev. C **23**, 2538 (1981); **25**, 677 (1982).
[10] R. Tamagaki, Prog. Theor. Phys. **39**, 91 (1968).
[11] R. B. Wiringa, V. G. J. Stoks, and R. Schiavilla, Phys. Rev. C **51**, 38 (1995); H. Kamada *et al*., Phys. Rev. C **64**, 044001 (2001).
[12] R. Thompson, M. Lemere, and Y. C. Tang, Nucl. Phys. **A286**, 53 (1977).
[13] H. Kanada, T. Kaneko, S. Nagata, and M. Nomoto, Prog. Theor. Phys. **61**, 1327 (1979).
[14] S. Aoyama, S. Mukai, K. Katō, and K. Ikeda, Prog. Theor. Phys. **93**, 99 (1995).
[15] K. Varga and Y. Suzuki, Phys. Rev. C **52**, 2885 (1995); Y. Suzuki and K. Varga, *Lecture Notes in Physics: Stochastic Variational Approach to Quantum-Mechanical Few-Body Problems* (Springer, Berlin, 1998), Vol. 54.
[16] Y. Suzuki, J. Usukura, and K. Varga, J. Phys. B **31**, 31 (1998); K. Varga, Y. Suzuki, and J. Usukura, Few-Body Syst. **24**, 81 (1998).
[17] N. W. Schellingerhout, L. P. Kok, S. A. Coon, and R. M. Adam, Phys. Rev. C **48**, 2714 (1993).
[18] K. Arai, Y. Suzuki, and K. Varga, Phys. Rev. C **51**, 2488 (1995).
[19] J. Usukura, K. Varga, and Y. Suzuki, Phys. Rev. A **58**, 1918 (1998).
[20] E. Hiyama, Y. Kino, and M. Kamimura, Prog. Part. Nucl. Phys. **51**, 223 (2003).
[21] Y. Suzuki and J. Usukura, Nucl. Instr. and Meth. in Phys. Res. B **171**, 67 (2000).
[22] V. I. Kukulin and V. N. Pomerantsev, Ann. Phys. **111**, 330 (1978).
[23] Y. Suzuki and K. Ikeda, Phys. Rev. C **38**, 410 (1988).
[24] D. Baye, M. Kruglanski, and M. Vincke, Nucl. Phys. **A573**, 431 (1994).
[25] W. Horiuchi and Y. Suzuki, Phys. Rev. C **73**, 037304 (2006); **74**, 034311 (2006).
[26] C. R. Ottermann *et al*., Nucl. Phys. **A436**, 688 (1985).
[27] Particle Data Group, J. Phys. G: Nucl. Part. Phys. **33**, 1 (2006).
[28] R. Sánchez *et al*., Phys. Rev. Lett. **96**, 033002 (2006).
[29] M. Puchalski, A. M. Moro, and K. Pachucki, Phys. Rev. Lett. **97**, 133001 (2006).
[30] L.-B. Wang *et al*., Phys. Rev. Lett. **93**, 142501 (2004).
[31] C. W. de Jager, H. de Vries, and C. de Vries, At. Data Nucl. Data Tables **14**, 479 (1974).
[32] T. Myo, K. Katō, and K. Ikeda, Prog. Theor. Phys. **113**, 763 (2005).
[33] S. C. Pieper, R. B. Wiringa, and J. Carlson, Phys. Rev. C **70**, 054325 (2004).
[34] K. Arai, Y. Suzuki, and R. G. Lovas, Phys. Rev. C **59**, 1432 (1998).
[35] M. Theeten, D. Baye, and P. Descouvemont, Phys. Rev. C **74**, 044304 (2006).
[36] G. D. Alkhazov *et al*., Phys. Rev. Lett. **78**, 2313 (1997).
[37] P. Egelhof for the IKAR Collaboration, Prog. Part. Nucl. Phys. **46**, 307 (2001).
[38] A. Ozawa, T. Suzuki, and I. Tanihata, Nucl. Phys. **A693**, 32 (2001).
[39] J. Cederberg *et al*., Phys. Rev. A **57**, 2539 (1998).
[40] David M. Bishop and Lap M. Cheung, Phys. Rev. A **20**, 381 (1979).
[41] G. G. Ryzhikh, R. A. Eramzhyan, V. I. Kukulin, and Yu. M. Tchuvil'sky, Nucl. Phys. **A563**, 247 (1993).
[42] R. B. Wiringa and R. Schiavilla, Phys. Rev. Lett. **81**, 4317 (1998).
[43] M. Bernheim *et al*., Nucl. Phys. **A365**, 349 (1981).
[44] K. I. Blomqvist *et al*., Phys. Lett. **B424**, 33 (1998).
[45] R. Schiavilla, R. B. Wiringa, Steven C. Pieper, and J. Carlson, Phys. Rev. Lett. **98**, 132501 (2007).